

Numerical Analysis of the Atmospheric Boundary-Layer Turbulence Influence on Microscale Transport of Pollutant in an Idealized Urban Environment

Tim Nagel, Robert Schoetter, Valéry Masson, Christine Lac, Bertrand Carissimo

▶ **To cite this version:**

Tim Nagel, Robert Schoetter, Valéry Masson, Christine Lac, Bertrand Carissimo. Numerical Analysis of the Atmospheric Boundary-Layer Turbulence Influence on Microscale Transport of Pollutant in an Idealized Urban Environment. Boundary-Layer Meteorology, In press, 10.1007/s10546-022-00697-7 . meteo-03625286

HAL Id: meteo-03625286

https://meteofrance.hal.science/meteo-03625286

Submitted on 30 Mar 2022

HAL is a multi-disciplinary open access archive for the deposit and dissemination of scientific research documents, whether they are published or not. The documents may come from teaching and research institutions in France or abroad, or from public or private research centers.

L'archive ouverte pluridisciplinaire **HAL**, est destinée au dépôt et à la diffusion de documents scientifiques de niveau recherche, publiés ou non, émanant des établissements d'enseignement et de recherche français ou étrangers, des laboratoires publics ou privés.

Noname manuscript No.
(will be inserted by the editor)

Numerical Analysis of the Atmospheric Boundary-Layer Turbulence Influence on Microscale Transport of Pollutant in an Idealized Urban Environment

Tim Nagel · Robert Schoetter · Valéry Masson · Christine Lac · Bertrand Carissimo

Received: DD Month YEAR / Accepted: DD Month YEAR

Abstract The mesoscale atmospheric model Meso-NH is used to investigate the influence of the mesoscale atmospheric turbulence on the mean flow, turbulence, and pollutant dispersion in an idealized urban-like environment, the array of containers investigated during the Mock Urban Setting Test field experiment. First, large-eddy simulations are performed as in typical computational fluid dynamics-like configurations, i.e., without accounting for the atmospheric boundary-layer (ABL) turbulence on scales larger than the building scale. Second, in a multiscale configuration, turbulence of all scales prevailing in the ABL is accounted for by using the grid-nesting approach to downscale from the meso- to the microscale. The building-like obstacles are represented using the immersed boundary method and a new turbulence recycling method is used to enhance the turbulence transition between two nested domains.

Upstream of the container array, flow characteristics such as wind speed, direction and turbulence kinetic energy are well reproduced with the multiscale configuration, showing the efficiency of the grid-nesting approach in combination with turbulence recycling for downscaling from the meso- to the microscale. Only the multiscale configuration is able to reproduce the mesoscale turbulent structures crossing the container array. The accuracy of the numerical results is evaluated for wind speed, wind direction, and pollutant concentration. The microscale numerical simulation of wind speed and pollutant dispersion in an urban-like environment benefits from taking into account the ABL turbulence. However, this benefit is significantly less im-

T. Nagel, R. Schoetter, V. Masson, C. Lac
Centre National de Recherches Météorologiques (Météo-France), 42 avenue Gaspard Coriolis 31057 Toulouse, France.
E-mail: tim.nagel@meteo.fr; robert.schoetter@meteo.fr

B. Carissimo
CEREA, Teaching and Research Center in Atmospheric Environment (ENPC/EDF R&D), 6 Quai Watier 78400 CHATOU Cedex, France.

portant than what is described in the literature for the Oklahoma City Joint Urban 2003 real case. The present study highlights that pollutant dispersion simulation improvement when accounting for ABL turbulence is dependent on the specific configuration of the city.

Keywords Idealized urban environment · Immersed boundary method · Large-eddy simulations · Meso–Microscale interaction · Pollutant transport

1 Introduction

Cities have an impact on the atmospheric boundary-layer (ABL) by modifying its dynamical and thermodynamical structure. They also release a significant amount of pollutant into the atmosphere. The concentration and the residence time of pollutants in cities are strongly influenced by their geometrical complexity. High values of pollutant concentration and residence time result in environmental and health issues. According to the World Health Organization, air pollution caused 4.2 million premature deaths worldwide in 2016[1]. Air quality has therefore become a point of particular interest for inhabitants and policy makers.

The precise quantification of atmospheric flows, pollutant transport, and dispersion in cities is a major modelling challenge (Dauxois et al. 2021). To accurately resolve atmospheric flows and pollutant dispersion in cities it is necessary to account for small-scale fluid dynamical and radiative processes over a complex and heterogeneous terrain including buildings of different dimensions, shapes and materials, streets of various spacing, trees in the streets, parks, and potentially water (river and ponds).

Computational fluid dynamics (CFD) is a very convenient and widely used tool for urban air pollution studies. Reviews by Tominaga and Stathopoulos (2013) or Blocken (2015) show the variety of CFD models available [with turbulence closure from Reynolds-averaged Navier–Stokes (RANS) to large-eddy simulations (LESs)] and some of their applications (from pedestrian comfort to air quality studies). The main advantage of CFD models is their ability to deal with very fine resolution and to resolve complex geometries. With the increase of computational power, CFD models have been applied to areas as large as a part of a city (the downtown of Oklahoma City, for instance, as in García-Sánchez et al. 2018). However, despite recent improvements (García-Sánchez and Gorlé 2018; García-Sánchez et al. 2018), the CFD models' boundary conditions do not represent the inherent variability of the real ABL. This issue is considered as one of the CFD models' bottlenecks (Dauxois et al. 2021).

Numerically reproducing atmospheric flow and pollutant dispersion in the urban environment can also be done through multiscale numerical weather prediction (NWP) models such as the Weather Research and Forecasting (WRF, Skamarock et al. 2008) or Meso-NH (where NH means non-hydrostatic, Lac

[1] https://www.who.int/news-room/fact-sheets/detail/ambient-(outdoor)-air-quality-and-health

et al. 2018). Advances in computational resources allow performance of microscale simulations of the ABL at LES resolutions (e.g., Couvreux et al. 2020). Provided that meteorological variables are correctly downscaled from mesoscale to microscale resolutions, e.g., using a grid-nesting approach, multiscale NWP models appear as a suitable tool to study the effect of ABL turbulence on the microscale atmospheric flow and pollutant dispersion in an urban environment. A major issue lies in the terrain-following vertical coordinate system used in numerous NWP codes. When performing high-resolution simulations over complex terrain, numerical errors arise because of the grid distorsion (Zängl et al. 2004). By definition, there is no steeper slope than a vertical building facade. This issue can be overcome thanks to another numerical approach, the immersed boundary method (IBM), which is compatible with NWP models such as WRF (Lundquist et al. 2010, 2012) or Meso-NH (MNH-IBM, Auguste et al. 2019). Recently, Wiersema et al. (2020) performed mesoscale to microscale simulations of the Joint Urban 2003 (JU2003) field campaign in Oklahoma City (Allwine et al. 2004; Allwine and Flaherty 2006) with WRF using the IBM to represent the buildings. They have shown that the pollutant dispersion is better simulated when using a multiscale NWP model rather than a CFD-like model with idealized boundary conditions and a limited domain vertical extent. The study of Wiersema et al. (2020) is based on a real city experimental dataset. The complexity of this real city may generate difficulties in distinguishing between the general impact of buildings and other phenomena like channelling, local recirculation, or pollutant trapping due to a specific configuration of the city (Milliez and Carissimo 2007). Real cases can be simplified while keeping their main advantage, which is the realistic meteorological conditions. This is done through field experiments with an idealized city with regular array of rectangular obstacles, such as the Mock Urban Setting Test experiment (MUST, Biltoft 2001; Yee and Biltoft 2004).

In the present study, MNH-IBM is used to investigate the influence of the mesoscale atmospheric turbulence on the mean flow, the turbulence, and the pollutant dispersion in the MUST idealized urban-like environment. The influence of a limited vertical extent, which is usually used in CFD simulations (Blocken 2015), is also investigated. Three configurations are studied: two CFD-like configurations, with and without limited vertical extent, where a velocity profile is prescribed at the boundaries and a multiscale configuration, where the large-scale atmospheric turbulence prevailing in the ABL is accounted for, thanks to grid-nested domains with increasing horizontal resolution. A new turbulence recycling method is also introduced to enhance the scale transition of the ABL turbulence.

Below, the model is presented in Sect. 2, the MUST experiment and the numerical configurations are detailed in Sect. 3 and Sect. 4, respectively, and the results are presented in Sect. 5. A discussion is proposed in Sect. 6. At the end, a summary of findings is given and some future directions are discussed.

2 Mesoscale Atmospheric Model Meso-NH for Obstacle-Resolving Simulations

2.1 The Meso-NH Model

The Meso-NH model (Lac et al. 2018) is a non-hydrostatic research atmospheric model, able to simulate atmospheric flows from the mesoscale (tens of kilometres and day-long phenomena) to the microscale (metres and second-long phenomena). The Meso-NH model is parallelized (Jabouille et al. 1999) and able to perform dynamical downscaling using the grid-nesting approach (Stein et al. 2000). The governing equations are based on the conservation laws for mass, momentum, energy, and on the ideal gas law. The Meso-NH model uses the anelastic approximation of the pseudo-incompressible system of Durran (1989), filtering the elastic effects from acoustic waves.

The domain is spatially discretized using the C-grid of Arakawa (Mesinger and Arakawa 1976). A conformal projection system and a regular grid size ($\Delta_x = \Delta_y = \Delta$) are used for the horizontal directions. The vertical grid is based on the terrain-following coordinates of Gal-Chen and Somerville (1975) which fit non-plane surfaces.

In the present study, a LES framework is used to estimate the Reynolds Stress term in the momentum equation. The LES closure is performed by the 1.5-order closure scheme described in Cuxart et al. (2000). This closure is based on the calculation of the subgrid turbulence kinetic energy ($e_{sb} = 1/2(\overline{u'^2}+\overline{v'^2}+\overline{w'^2})$, where u', v', and w' are the x-, y-, and z-turbulence velocity components) through a prognostic equation and on a diagnostic adaptative mixing length (Honnert et al. 2021).

For the wind advection, Meso-NH uses either CEN4TH, a fourth-order centred scheme, or WENO5, a fifth-order weighted essentially non-oscillatory scheme. Explicit Runge–Kutta schemes are used for time integration (Lunet et al. 2017). The CEN4TH advection scheme should be used with a fourth-order Runge–Kutta (RKC4) time marching whereas WENO5 can be used together with a five-stage third-order Runge–Kutta (RK53) scheme. Explicit numerical diffusion is not appropriate with WENO5, whereas CEN4TH requires numerical diffusion, which is characterized by the e-folding time t_c of $2\Delta_x$ waves.

The advection of a prognostic scalar such as the pollutant is made by a piecewise parabolic method (PPM) based on the original Colella and Woodward (1984) scheme with monotonicity constraints modified by Lin and Rood (1996). The temporal algorithm of PPM is forward-in-time. Explicit numerical diffusion is not used either with the PPM scheme.

2.2 The Immersed Boundary Method in Meso-NH

Since the numerical solvers in Meso-NH enforce conservation on structured grids, they cannot handle body-fitted grids with steep topological gradients.

This is a common issue for meteorological models. Explicitly modelling the fluid–solid interaction in the urban roughness sublayer, which extends up to 2–5 times the characteristic building height (Roth 2000) is necessary to capture the relevant processes for the urban climate. To this end, a version of Meso-NH including the IBM to represent the buildings, MNH-IBM, has been developed by Auguste et al. (2019). The MNH-IBM version is currently restricted to cartesian grids and flat terrains.

Within the MNH-IBM framework, the numerical domain is divided between two distinct regions: a fluid region where the classical fluid conservation laws are applied and a solid region having a volume similar to the embedded obstacles. The interface between the two regions is defined by a continuous level-set function (Sussman et al. 1994), ϕ. The absolute value of ϕ gives the minimal distance between a grid point and the interface. The sign of ϕ allows for distinguishing between the solid ($\phi > 0$) and the fluid ($\phi < 0$) region. The level-set function is restricted to non-moving interfaces and is not time-dependent, which is not an issue when it comes to modelling urban environments.

Among the various IBM methods, a review can be found in Iaccarino and Verzicco (2003) and Kim and Choi (2019), the fine resolution required close to the interface led Auguste et al. (2019) to adopt an IBM method based on the discrete forcing approach for MNH-IBM. The boundary conditions are specified at the immersed interface. This is achieved by forcing the conservation equations at the vicinity of the embedded solid surfaces via two Cartesian grid methods, a ghost-cell technique (Tseng and Ferziger 2003) and the cut-cell technique (Yang et al. 1997). The ghost-cell technique corrects the explicit-in-time schemes such as the advection and the diffusion schemes. It also computes the prognostic variables (velocity, temperature, and e_{sb}) in the immersed solid volume to satisfy the required boundary conditions at the interface. As an example, a local log law with the appropriate material roughness is imposed for the tangential velocity. The cut-cell technique corrects the pressure solver and ensures the incompressibility constraint by modifying the right-hand side of the Poisson equation. Finally, an iterative procedure is applied on the modified Poisson equation to ensure the interface non-permeability (Auguste et al. 2019).

The MNH-IBM implementation has been validated by Auguste et al. (2019) for the MUST idealized urban-like environment, without pollutant transport, realistic incoming turbulence or grid-nesting. In this study, MNH-IBM reproduced with reasonable accuracy the observed mean flow and turbulent fluctuations within the urban roughness sublayer. The MNH-IBM code has also been used to reproduce the dispersion of the pollutants plume generated by the AZF (AZotes Fertilisants) fertilizer production plant explosion in Toulouse (France) in September 2001 (Auguste et al. 2020). The model presented a realistic plume dispersion and simulated a limited population's exposure to pollution, which appeared to be in good agreement with the health studies performed on the AZF explosion.

2.3 The Turbulence Recycling in Meso-NH

One of the main bottlenecks encountered when performing multiscale LES simulations on nested grids is generating proper turbulence in the ABL. Indeed, a development fetch is needed within each domain to allow for the cascade of eddies of different scales in the inertial subrange to adapt to the new resolution (Muñoz-Esparza et al. 2014). Realistic turbulent inflow conditions must be generated to reduce this fetch. This has been an extensive research field over the last thirty years and numerous methods have been proposed. Among them, two are widely used: the cell perturbation method (Muñoz-Esparza et al. 2014, 2015), and recycling methods adapted from the original proposition of Lund et al. (1998). In the present study, the recycling method has been chosen for the sake of simplicity in the implementation.

The idea behind the recycling method of Lund et al. (1998) is simple. The prognostic variable fluctuations from a vertical plane parallel to the inflow boundary are calculated, extracted, and added to the variable field at the inlet. In several LES models, such as the Parallelized Large-Eddy Simulation Model (PALM, Maronga et al. 2015), the recycling method uses the modifications to the original proposition of Lund et al. (1998) introduced by Kataoka and Mizuno (2002): the fluctuations are calculated with respect to a constant altitude line average in the recycling plane. This method has been successfully used to study configurations with urban topography (Park et al. 2015a,b). However, as mentioned by Muñoz-Esparza et al. (2015), this method may present issues when the flow direction changes and is not easily generalized for multiple inflow boundaries. Moreover, performing a spatial average to calculate the fluctuations is not adapted to inhomogeneous main flow and turbulence.

In the present study, an alternative recycling method is introduced: the prognostic variable fluctuations from a vertical plane parallel to the inflow boundary are calculated with respect to a moving temporal average and these fluctuations are added to the prognostic variable field at the inlet. First, it must be ensured that the turbulence is resolved down to $M\Delta$ in the father model, M being ideally equal to 4 or 6, depending on the effective resolution of the father model (Skamarock 2004). The effective resolution of a model is the minimum wavelength correctly simulated by the model. In the nested son domain, the time window for the calculation of the moving temporal average (T_{recycl}) has to be sufficiently large for the fluid to be advected over a distance corresponding to about $M\Delta$ in the father model. Furthermore, to save computational time and memory, the variable average is calculated with a limited number of son domain timesteps (N) over T_{recycl}. The value of N should be sufficiently high to reduce the statistical uncertainty of the calculated moving average and sufficiently low in terms of memory requirements, since the N values for each grid point in the recycling plane need to be kept in memory.

Figure 1 shows a domain where inflow boundary conditions may be imposed at each lateral side (north, east, south, west). For the sake of clarity, we consider in the following that the flow is incoming from the west boudary, i.e.,

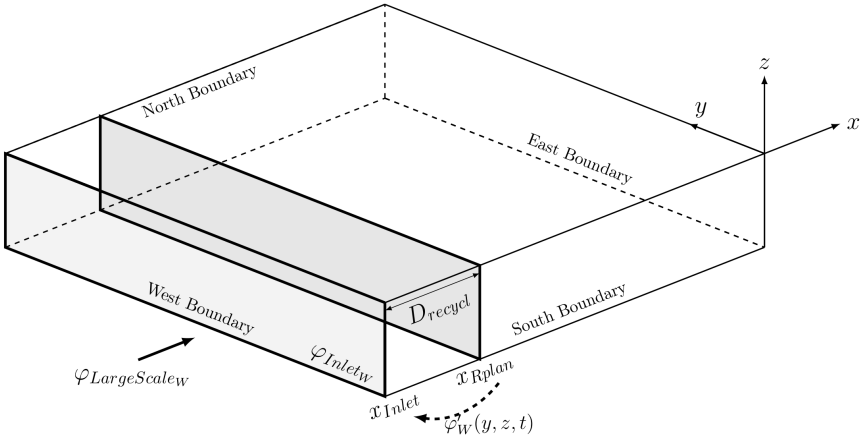


Fig. 1 Sketch of the turbulence recycling method used to generate turbulent inflow. For clarity, only the recycling of fluctuations at the west boundary is shown, but the same method applies on the four lateral sides

the recycling method is only applied on the west boundary. If needed, the same method could apply on the four lateral sides. A wind vector that is not aligned with the grid axis will thus be recycled on two sides. Considering the prognostic variable at the west boundary (W) $\varphi_W \in [u, v, w]$, the fluctuations φ'_W are calculated in the recycling plane being located at a distance D_{recycl} from the inlet. In the present work, since we are working on near-neutral cases, only the three velocity components are recycled. For other configurations, prognostic variables such as the temperature can be recycled. The fluctuations calculation reads:

$$\varphi'_W(y,z,t) = \varphi_W(x_{Rplan}, y, z, t) - \overline{\varphi_W(x_{Rplan}, y, z)}, \tag{1}$$

where $\varphi_W(x_{Rplan}, y, z, t)$ and $\overline{\varphi_W(x_{Rplan}, y, z)}$ are the instantaneous and the time averaged prognostic variable in one point of the recycling plane, respectively.

The value of $\varphi'_W(y,z,t)$ is added to the corresponding inflow prognostic variable, φ_{Inlet_W} :

$$\varphi_{Inlet_W}(y,z,t) = \varphi_{LargeScale_W}(y,z,t) + \varphi'_W(y,z,t)\beta\psi_W(y,z,t), \tag{2}$$

where $\varphi_{LargeScale_W}$ is the variable field imposed at the boundary, $\beta \in$ [0.1-0.25] a weighting coefficient preventing calculation divergence, and $\psi_W(y,z,t)$ an inflow damping function:

$$\psi_W \rightarrow \begin{cases} 1 & ; \text{if } T_{BV} > T_{BV_{max}} \\ \dfrac{(T_{BV} - T_{BV_{min}})}{(T_{BV_{max}} - T_{BV_{min}})} & ; \text{if } T_{BV_{min}} \leq T_{BV} \leq T_{BV_{max}} \\ 0 & ; \text{if } T_{BV} < T_{BV_{min}} \end{cases}, \tag{3}$$

where T_{BV} is the calculated Brunt–Väisälä period, and $T_{BV_{max}}$ and $T_{BV_{min}}$ are maximal and minimal allowed values of the Brunt–Väisälä period. Here, $T_{BV_{min}} = 2T_{BV_{nn}}$ and $T_{BV_{max}} = 3T_{BV_{nn}}$, where $T_{BV_{nn}} \approx 90$ s is the estimated Brunt–Väisälä period for the U.S. Standard Atmosphere.

The ψ_W function is calculated at the inlet; it is equal to 1 in neutral or near-neutral layers (e.g., in the boundary layer) and is linearly damped to 0 in stable layers. Its purpose is twofold: filtering the fluctuations due to gravity waves and preventing the imposed fluctuations to be affected by a potential increase in boundary-layer height between the recycling plane and the inlet. The proposed recycling method has been successfully validated in Sect. 5.1 for a neutral ABL.

3 The Mock Urban Setting Test Experiment

3.1 Description

The Mock Urban Setting Test (MUST) experiment (Biltoft 2001; Yee and Biltoft 2004) is a near full-scale measurement campaign conducted during the month of September 2001 in Utah's West desert, at the U.S. Army Dugway Proving Ground (40° 12.606' N, 113° 10.635' W). The site is located 1310 m above the mean sea level and can be considered flat. The MNH-IBM model, limited to Cartesian grids, can therefore be used to reproduce this experiment.

The MUST experimental campaign objective was twofold: study the dispersion of a passive tracer through a large array of building-like obstacles and provide reference data for the validation of numerical models for dispersion of pollutants in urban areas.

Figure 2 shows a sketch of the experimental configuration. The MUST idealized urban-like environment consists of a near-regular array of 10 × 12 ship-containers. Their dimensions are 2.42 m in width (L_x), 12.9 m in length (L_y), and 2.54 m in height (H) except for the one identified as H5, which is 2.44 m wide, 6.1 m long, and 3.51 m high. The horizontal averaged distance between the containers is 12.9 m in the x-direction and 7.9 m in the y-direction. The array axis forms an angle of 30° to the north. The desert vegetation surrounding the containers has an aerodynamic roughness length $z_0 = 0.045$ m (Yee and Biltoft 2004).

The MUST experimental procedure consists of 900-s-long releases of propylene (C_3H_6). This procedure has been repeated for different incoming wind directions and pollutant release locations; 21 cases are presented in Yee and Biltoft (2004). The locations of the different instruments used for comparison with model results in the present study are given in Fig. 2. The velocity and turbulence measurements have been performed using two- and three-dimensional sonic anemometers. They were placed at different heights upwind (mast S), downwind (mast N), within and above the container array. Concerning the pollutant, 72 detectors have been used to measure its concentration within and above the array. Horizontally, 40 photo-ionization detectors (PIDs)

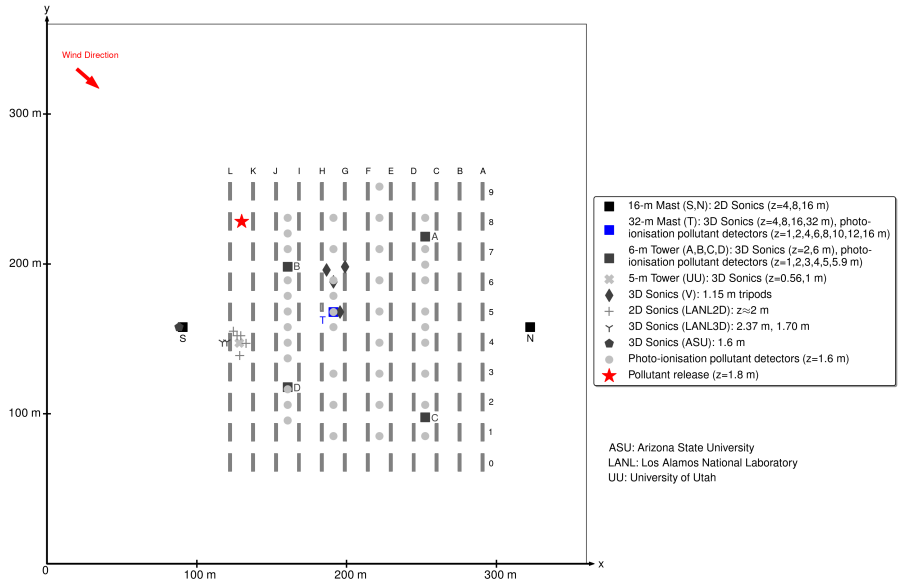


Fig. 2 Sketch of the MUST experiment including the location of the different instruments. The figure is adapted from Yee and Biltoft (2004) and Milliez and Carissimo (2007)

were located on four lines (light grey dots in Fig. 2) at height $z = 1.6$ m. Eight PIDs were mounted on the 32-m tower (T) and six ultraviolet ion collectors (UVICs) were mounted on each of the four 6-m towers (A, B, C, D) to obtain vertical pollutant concentration profiles.

3.2 Selected Case

We reproduce the MUST case number 2681829, starting 25 September 2001 at 1830 LT (local time = UTC−6 h). It was chosen because the atmosphere is in a near-neutral state, the Obukhov length (L_{MO}) being 28,000 m.

In order to prevent the results from being influenced by the unsteadiness of the atmospheric conditions, previous CFD simulations of the MUST case (Milliez and Carissimo 2007; Dejoan et al. 2010) were compared with the 200 s quasi-steady periods extracted by Yee and Biltoft (2004) within each 900-s plume dispersion experiment. As the focus of the present study is to investigate the influence of the ABL turbulence on the wind conditions and pollutant transport in the container array, the complete 900-s time period of pollutant release is investigated.

Table 1 gives information on the chemical substance release, the mean flow and the turbulence characteristics. The mean incident wind direction angle is equal to -40° with respect to the x-direction (Fig. 2). The tracer gas is released in the upstream part of the container array (Fig. 2, red star symbol) at a height of 1.8 m and at a constant flowrate of 225 L min^{-1}.

Table 1 Information on chemical substance release, main flow, and turbulence characteristics. The official case name is its date in the Julian calendar, 2681829 (25/09/2001). It is also named "trial 11" in Yee and Biltoft (2004). Here, $\overline{U_{04}}$ is the time-averaged wind speed, $\overline{\alpha_{04}}$ is the time-averaged wind mean direction at 4 m height on the upwind mast S, Q is the tracer release rate at the source, and x_s, y_s, z_s is the location of the source with respect to the coordinate system defined in Fig. 2

Start Time (LT)	$\overline{U_{04}}$ (m s^{-1})	$\overline{\alpha_{04}}$ (°)	L_{MO} (m)	(x_s, y_s, z_s) (m, m, m)	Q (L min^{-1})
1830	7.9	-40	28,000	(129.87, 228.35, 1.8)	225

4 Numerical Configurations

Three numerical configurations are studied. The MNH-IBM code is first used as in a typical CFD configuration, i.e., without accounting for the large-scale ABL turbulence. The first CFD-like configuration has a limited vertical extension of 40 m, whereas the second configuration simulates the entire ABL and extends up to 3000 m above ground level (a.g.l.) (i.e., 4310 m above mean sea level). In the third configuration, the large-scale atmospheric turbulence prevailing in the ABL is accounted for, thanks to nested domains with increasing horizontal resolution. In all configurations, the pollutant is considered as a passive scalar and its density difference with air is not accounted for, since the maximum pollutant concentrations are very small.

4.1 Computational Fluid Dynamics-like Configurations

The first CFD-like configuration (called CFD40) intends to reproduce what is typically done in obstacle-resolving scale CFD simulations. Two important simplications are performed. First, the observed wind profile is imposed at the boundary. Second, the top of the domain is fixed at $z \approx 40$ m, which corresponds approximatively to sixteen times the obstacles height. A domain top much lower than the ABL height is common in urban CFD simulations; the best practice guideline given by Franke et al. (2011) recommends using at least a domain six times higher than the tallest building.

Figure 3 schematically represents the CFD40 configuration: the containers are within a 360 m side square domain. The mesh is cartesian, with a horizontal resolution $\Delta_x = \Delta_y = 0.3$ m. In the vertical direction, for $z < 6$ m the vertical grid size is constant and $\Delta_z = 0.3$ m. Above 6 m, it increases with a constant geometric ratio of 1.095. The blockage ratio of the obstacles and the distance from the boundaries of the computational domain to the container array respect the Franke et al. (2011) guideline.

A steady velocity profile is imposed at the domain boundaries. It is constructed by fitting a log-law to the S tower observations, which are upstream of the container array. The incoming flow has a mean horizontal angle of -40° with respect to the x-direction, it only enters in the domain by the west and north boundaries.

The containers are represented with the IBM. The ground friction of the surrounding vegetation, characterized by an aerodynamic roughness length $z_0 = 0.045$ m, is modelled with the externalized surface scheme SURFEX (Masson et al. 2013). The turbulent fluxes of sensible and latent heat at the surface are prescribed as 0.0 W m^{-2}.

The turbulence recycling method is used at the west and north boundaries in order to generate a turbulent incoming flow. Here, $\beta = 0.25$ and since there is no father domain, a very low value of $T_{recycl} = 56$ corresponding to 1.12 s is chosen. The recycling plane is placed 30 m from the boundaries. As shown in Fig. 3, the velocity turbulent fluctuations are calculated in the vertical planes x_{Rplan_W} and y_{Rplan_N} and added to the inflow velocity field at the west and north boundaries, respectively. In this CFD-like configuration, the incoming flow contains small-scale turbulent structures only. It is therefore not representative of the ABL turbulence.

The WENO5 and RK53 schemes are used for the wind advection and the time marching. The WENO5 scheme has been selected because it is well adapted to sharp gradient areas (Lunet et al. 2017). Furthermore, the CFD40 configuration has no absorbing layer in the upper part of the domain as this case is purely neutral.

The second CFD-like configuration, named hereafter CFD3000, presents two differences compared to CFD40. First, the domain extends vertically to 3000 m a.g.l. Similarly to CFD40, for $z < 6$ m, the vertical grid size is constant with $\Delta_z = 0.3$ m. Above 6 m, the vertical grid size increases with a constant geometric ratio of 1.095 until Δ_z reaches 50 m. The case is near neutral up to 1500 m a.g.l. where an inversion layer is imposed. A Rayleigh relaxation layer is located above $z = 2000$ m to damp gravity waves. Secondly, since a logarithmic profile up to 3000 m a.g.l. is not a sustainable hypothesis, the CFD3000 case is forced with a velocity profile extracted from the multiscale configuration (Sect. 4.2).

For the two cases, the ceiling of the domain is rigid, corresponding to a free-slip condition. A summary of both CFD-like numerical configurations' main parameters is given in Table 2.

4.2 Multiscale Configuration

For the multiscale configuration (MSC), the mesoscale turbulence prevailing in the ABL is accounted for by using four nested domains with increasing horizontal resolution (Fig. 4). A one-way grid-nesting approach is used: the father domain variables influence the son domain variables but not vice-versa. The coarsest domain, D1, is a 76.8 km side square. It has a horizontal resolution of 96 m. Cyclic boundary conditions are employed for D1, therefore, from a physical point of view, its horizontal extent is infinite. Due to its coarse resolution, only the largest eddies of the neutral ABL are resolved in D1. The flow results from a balance between the Coriolis force, a geostrophic wind which represent the large scale pressure gradient and the surface friction. The grid-

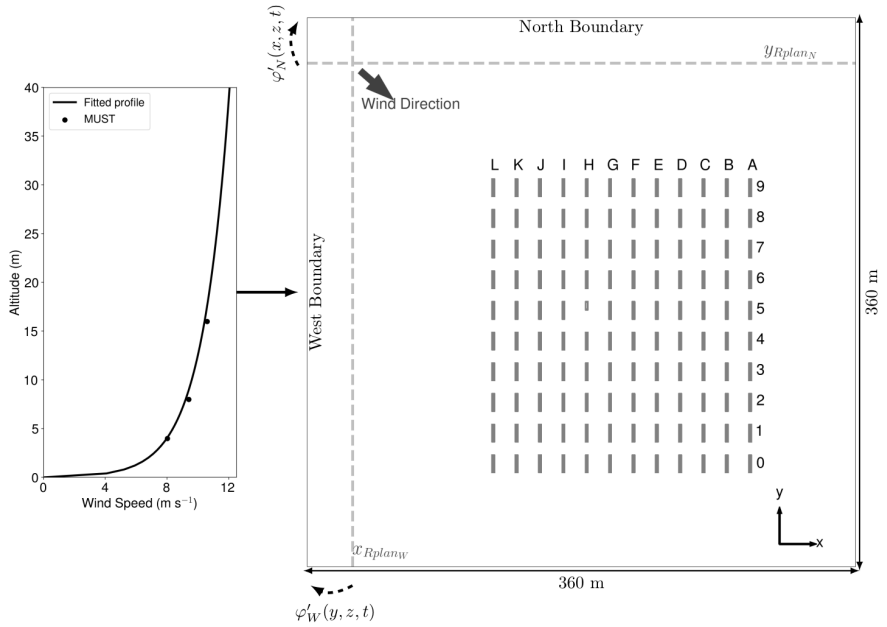


Fig. 3 Domain extent and inflow wind profile for the CFD40 configuration. A logarithmic velocity profile based on the experimental measurements profile is prescribed at the west and north boundaries. The turbulence recycling method is applied at these boundaries

nesting method is used for the lateral boundaries of the three finer domains. The domains 2 (D2) and 3 (D3) are 19.2 km and 2.4 km side squares with a horizontal resolution of 24 m and 3 m, respectively. Finally, the finest domain, D4, has the horizontal dimensions and resolution of the CFD-like configurations domain (Sect. 4.1). The vertical extent of all the nested domains is 3000 m a.g.l. in order to simulate the entire ABL for this desert site in early autumn. The vertical grid and top boundary conditions are identical to the CFD3000 ones. The predominant wind direction being known, D3 and D4 are placed in the bottom right part (with respect to the cartesian system represented in Fig. 4) of their parent domain. This is a common method to reduce the transition fetch between two nested domains (e.g., Wiersema et al. 2020).

In all the domains, the ground friction is characterized by an aerodynamic roughness length $z_0 = 0.045$ m and modelled with the SURFEX scheme (Masson et al. 2013). Except for the domain top height, the vertical grid and the boundary conditions, D4 has the same characteristics as the single domain employed for the CFD-like configurations.

The turbulence recycling method is used to enhance the turbulence scale transition between two nested subdomains. In D2 and D3, as shown in Fig. 4, the velocity fluctuations are added to the large-scale velocity fields coming from the father domain at the west and north boundaries. It has been found

that between D3 and D4, the turbulence scale transition naturally happens within a very reduced fetch. The turbulence recycling is therefore not used in D4.

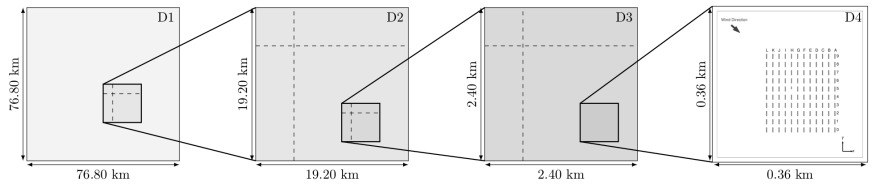


Fig. 4 Illustration of the MSC approach. The recycling method is applied on the west and north boundaries of domains D2 and D3. The dashed lines indicate the positions of the recycling vertical planes

Numerically, CEN4TH/RKC4 is used for D1, D2, and D3 because is it the more appropriate combination to perform LES of the ABL (Lac et al. 2018). Similar to the CFD-like configurations, WENO5/RK53 is used for D4. In all domains, an inversion layer is imposed at $z = 1500$ m and a Rayleigh relaxation layer is located above $z = 2000$ m. A summary of the numerical configurations is given for each domain in Table 2.

Table 2 Numerical configurations main parameters. GW: geostrophic wind. FD: wind coming from the father domain. IWP: Idealized wind profile. EWP: wind profile extracted from MSC. t_c: e-folding time of the $2\Delta_x$ waves

Parameter	D1	D2	D3	D4	CFD40	CFD3000
Δ_x and Δ_y (m)	96	24	3	0.3	0.3	0.3
Timestep (s)	1.2	0.24	0.04	0.02	0.02	0.02
Time integration scheme	RKC4	RKC4	RKC4	RK53	RK53	RK53
Wind advection scheme	CEN4TH	CEN4TH	CEN4TH	WENO5	WENO5	WENO5
t_c (s)	1800	100	10	None	None	None
Boundary-conditions	Cyclic	Open	Open	Open	Open	Open
Wind boundary-conditions origin	GW	FD	FD	FD	IWP	EWP
Turbulence recycling	No	Yes	Yes	No	Yes	Yes

5 Results

5.1 Validation of the Turbulence Recycling Method

The turbulence recycling method described in Sect. 2.3 is here validated for the neutral conditions corresponding to the selected MUST case. For this purpose, a preliminary configuration is used, which is different from the MSC

as it includes only two nested domains. The domain 1 presented in Sect. 4.2 is the father domain. The son domain has the resolution of D2, but its side length is reduced to 9600 m. The CEN4TH/RKC4 set-up is employed in both domains.

A 200000-s simulation is conducted for D1, a simulation duration sufficient for the establishment of the geostrophic wind balance and the development of the largest eddies of the neutral ABL. The effective resolution of D1, defined via the turbulence spectrum in the inertial subrange is 4Δ (not shown but in agreement with Lac et al. 2018 for to the 4th-order advection scheme). In the son domain, the velocity fluctuations are added to the large-scale velocity fields coming from the father domain at the west and north boundaries. The fluctuations are calculated in vertical planes placed at 2400 m (equivalent to one fourth of the domain size) of the boundary. The velocity fluctuation average is calculated over $N = 28$ timesteps, which corresponds to 672 s.

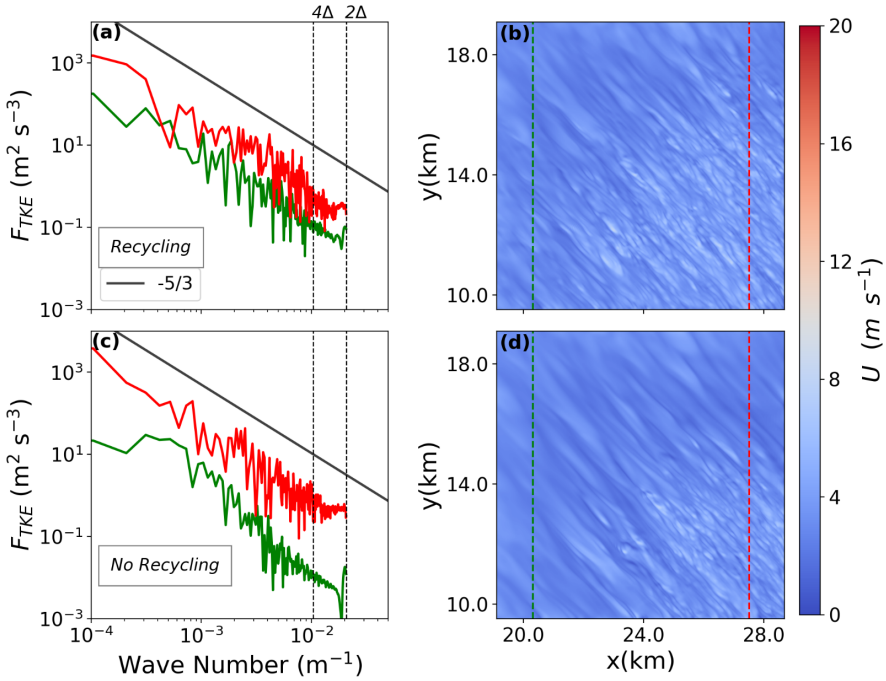


Fig. 5 The TKE spectrum at $z = 500$ m (**a**,**c**) and wind speed at $z = 1.5$ m (**b**,**d**) in the son domain after 30000 s of dynamics using the turbulence recycling method (**a**,**b**) or not (**b**,**c**). Green and red dashed lines in the right column show where the corresponding color TKE spectrum is calculated. The full black line in the spectrum plots is the Kolmogorov $-5/3$ slope

Figure 5 shows the effects of the turbulence recycling on the wind speed at $z = 1.5$ m (Fig. 5b, d) and the turbulence kinetic energy (TKE) spectrum at $z = 500$ m (Fig. 5a, c) in the son domain after 30000 s. For the wind speed at $z = 1.5$ m, when using the turbulence recycling method, small-scale turbulent structures are present in a large part of the domain, except close to the inlet boundaries. Without the turbulence recycling method, these small-scale turbulent structures are only present at the bottom right corner of the domain. These turbulent structures close to the ground change the incoming flow in the container array. The same transition improvement is found all along the vertical direction.

Green and red dashed lines in Fig. 5b and d show where the corresponding colour TKE spectrum is calculated. When using the turbulence recycling method, the turbulence is at scale in the son domain. By "at scale" we mean that the turbulence in the inertial subrange is well developed and that the turbulence spectrum follows Kolmogorov's $k^{-5/3}$ law until $4\Delta_x$. With the turbulence recyling method, this is true even close to the west and north boundaries (see the green spectrum). This is not the case without the turbulence recycling method, where the turbulence at scale is restricted to the areas close to the east and south boundaries.

The turbulence recycling method thus allows the reduction of the fetch and efficiently improves the turbulence scale transition when using nested grids.

5.2 Wind Speed, Wind Direction, and Turbulence Kinetic Energy in the Surface Layer Upstream of the Container Array

Figure 6 shows the 900-s-average vertical profiles in the surface layer of the wind speed (Fig. 6a), wind direction (Fig. 6b), and total TKE (Fig. 6c) at the S tower located upstream of the container array (Fig. 2).

Concerning both CFD-like configurations, the wind speed profiles match very well the observations from Yee and Biltoft (2004). The agreement is also satisfactory for the wind direction. The TKE is underestimated all along the vertical. It must however be recalled here that, contrary to RANS CFD models, no TKE boundary conditions can be imposed in Meso-NH. In these configurations, the TKE is mainly obtained thanks to the turbulence recycling method. A simulated TKE that is in the same order of magnitude as the experimental results remains therefore acceptable. The profiles are very similar between both CFD-like configurations, showing that the domain height has no impact on the incoming wind profile.

Concerning the MSC, the wind speed and the wind direction profiles are in very good agreement with the observations in the surface layer. The MSC's TKE profile agrees well with the observations. It shows that the turbulence is well captured upstream of the container array.

Figure 7 shows the temporal evolution of the wind speed and direction at tower S for the 900 s of the pollutant release, for $z = 4$ m and $z = 16$ m. The temporal resolution is 0.1 s for the numerical simulations and the observations.

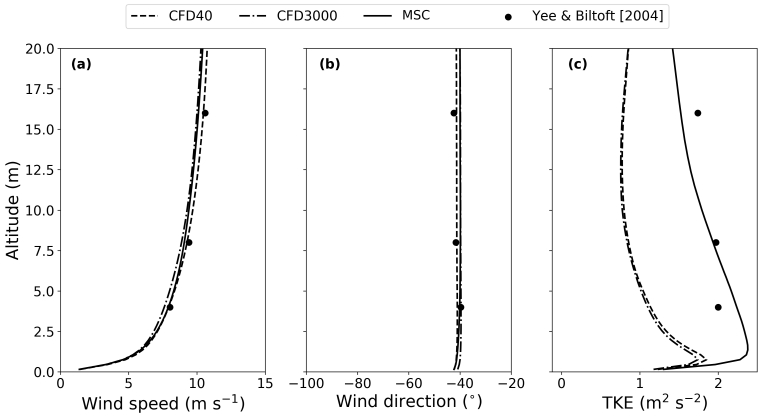


Fig. 6 Average (900 s) vertical profiles of wind speed (**a**), wind direction (**b**), and TKE (**c**) at the S tower location upstream of the container array (Fig. 2)

The observed wind direction variability is less important at $z = 16$ m than at $z = 4$ m. This is well captured by the two CFD-like and the MCSs. For the sake of clarity, only CFD40 is shown. The results are almost identical for CFD3000.

For a more quantitative comparison, the mean and standard deviation of the series are compared in Table 3. The time-averaged wind speed is in excellent agreement with the observations, especially for the CFD40 and the MSCs. At $z = 4$ m, CFD40 simulates an averaged wind direction slightly shifted about 2° to the right (from a wind flow point of view). On the contrary, at $z = 16$ m, MSC and CFD3000 (which is forced by a velocity profile extracted from MSC) simulate an average wind direction shifted about 2° to the left. However, the overall agreement remains very satisfactory for both configurations.

Both CFD-like configurations underestimate the standard deviation for each quantity, at both altitudes, whereas the agreement is very good for the MSC. This can also be seen in Fig. 7, where fluctuations in wind speed and wind direction are more monotonous for CFD40 and CFD3000 than for MSC. This is particularly visible at $z = 16$ m where the low-frequency oscillations are reproduced with the MSC only. These low-frequency variations are characteristic of large ABL turbulent eddies of several minutes time scale crossing the probes.

Figure 8 shows the instantaneous wind speed at $z = 1.6$ m in the four nested domains of the MSC. The recycling method is effective since the transition fetch is limited to about one quarter of the model domain distance to the west and north boundaries in D2 and D3. For both of these domains, the transition fetch is halved when using the turbulence recycling method (not shown). Furthermore, ABL turbulence is simulated upstream of the container array in D4. This is not the case for the CFD-like configurations (not shown).

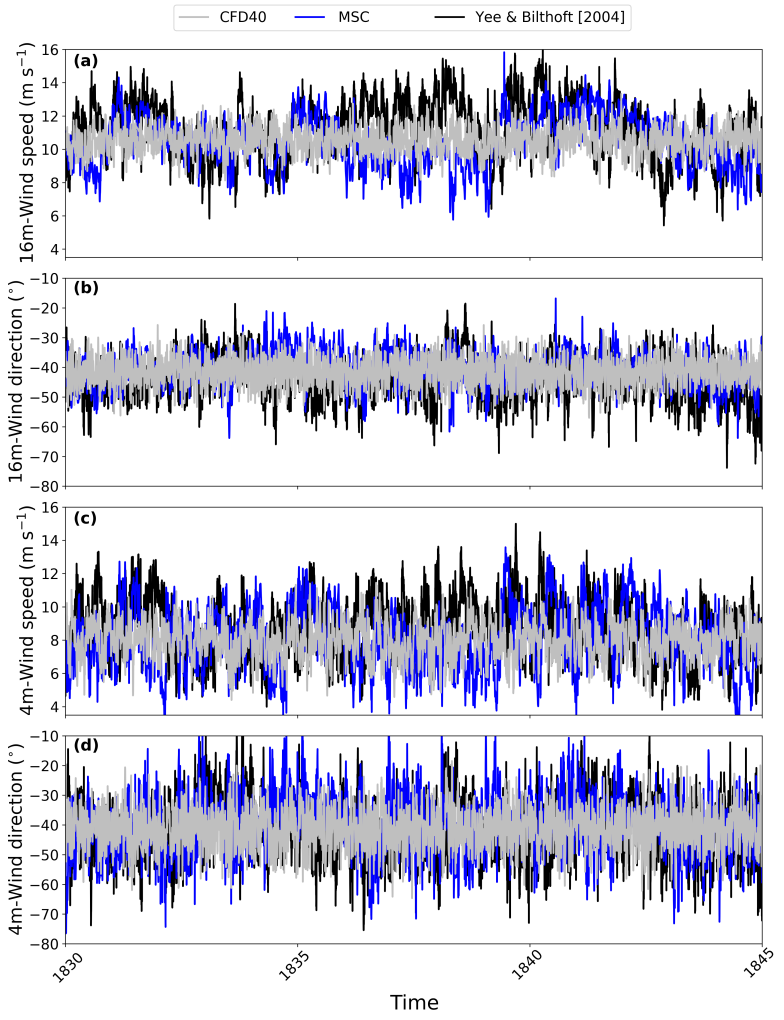


Fig. 7 Temporal evolution of the wind speed and wind direction at 16 m a.g.l. (**a**,**b**) and 4 m a.g.l. (**c**,**d**) for tower S located upstream of the container array. The temporal resolution is 0.1 s for the numerical simulations and the observations

The mean incoming wind conditions for the two CFD-like and multiscale configurations agree with the observations. The largest turbulent eddies occurring in the ABL are present in the MSC only. This allows investigation of the effects of the large ABL turbulent structures on the pollutant dispersion within the container array.

Table 3 Summary of the time average and standard deviation of the sample for the wind speed and direction at tower S located upstream of the container array. "Experiment" corresponds to the observations from Yee and Biltoft (2004)

Case -	$\overline{U_{04}}$ (m s^{-1})	$\sigma(U_{04})$ (m s^{-1})	$\overline{\alpha_{04}}$ (°)	$\sigma(\alpha_{04})$ (°)	$\overline{U_{16}}$ (m s^{-1})	$\sigma(U_{16})$ (m s^{-1})	$\overline{\alpha_{16}}$ (°)	$\sigma(\alpha_{16})$ (°)
Experiment	8.0	1.6	-39.7	8.6	10.6	1.5	-42.4	5.9
CFD40	8.0	1.1	-41.2	6.5	10.5	0.8	-41.5	4.5
CFD3000	7.7	1.1	-39.6	6.7	10.1	0.8	-40.0	4.5
MSC	8.1	1.9	-40.1	9.6	10.4	1.5	-40.5	5.8

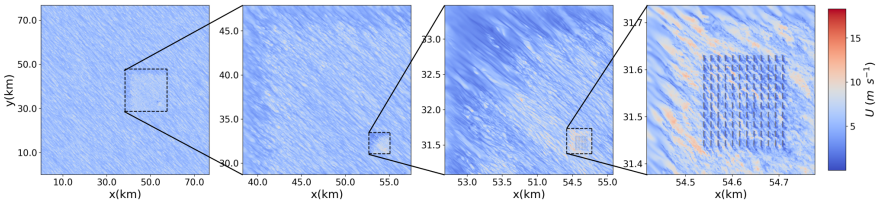


Fig. 8 Instantaneous ($t = 780$ s) wind speed at $z = 1.6$ m in the four nested domains of the MSC

5.3 Wind Speed, Wind Direction, and Turbulence Kinetic Energy Within and Above the Container Array

Figure 9 shows the 900-s-average vertical profiles of wind speed (Fig. 9a), wind direction (Fig. 9b), and TKE (Fig. 9c) at the mast T located within the container array (Fig. 2). The MSC agrees well with the observations all along the vertical. It is able to reproduce with high accuracy the wind speed reduction below $z = 10$ m due to the presence of the containers. Although less accurate, the CFD-like configurations also perform well below $z = 10$ m, but CFD40 overestimates the wind speed above $z = 10$ m whereas CFD3000 slightly underestimates it. Concerning CFD40, the overestimation is more pronounced at $z = 32$ m and is due to the unrealistic presence of a model top at $z = 40$ m.

The wind direction below $z = 3$ m, i.e., inside the container array, is similar for all configurations. Its values deviate from the upstream values of $-40°$ to reach $-100°$, indicating that, at mast T, the wind within the container array is almost aligned with the y-direction. This is due to the fact that mast T is located in the recirculation cell of a container. Directly above the container height the wind direction corresponds to the inlet wind direction ($\approx -40°$) for all configurations. This turning effect below the canopy height has been previously noticed by Yee and Biltoft (2004) and Milliez and Carissimo (2007).

All configurations present slight discrepancies in the vertical TKE profiles. The MSC and CFD40 configurations underestimate the TKE above $z = 10$ m and $z = 4$ m, respectively. In the container array, below $z = 4$ m, both configurations display similar TKE profiles but overall, the MSC agrees better with

the observations. The CFD3000 TKE profile matches the CFD40 one between 4 and 25 m. Above $z = 25$ m, CFD40 deviates because of the roof presence. Below $z = 4$ m, CFD3000 underestimates the TKE in a more pronounced way than CFD40.

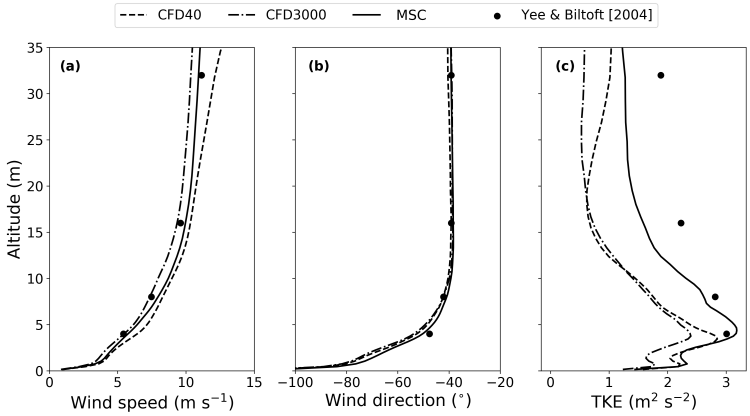


Fig. 9 Average (900 s) vertical profile of wind speed (**a**), wind direction (**b**), and TKE (**c**) at mast T located inside the container array (Fig. 2)

The overall good agreement between the presented numerical results and the literature shows that MNH-IBM and particularly the MSC are able to accurately simulate the average and standard deviation of wind speed and direction, and the TKE within and above the MUST container array.

5.4 Pollutant Dispersion

Figure 10 shows the pollutant concentration averaged over 900 s at $z = 1.6$ m for the CFD40 (Fig. 10a, c) and the MSC approaches (Fig. 10b, d). The coloured circles indicate the observed values at the 40 PIDs probes located at $z = 1.6$ m. The full lines represent the 0.1 parts per million (ppm) iso-line of pollutant concentration. The wind speed is represented with a quiver plot in Figs 10c and d. The CFD3000 results (not shown on Fig. 10) are almost identical to the CFD40 ones.

The spread of the plume differs between the configurations. The CFD-like configurations are less dispersive than the multiscale one and underestimate the lateral plume spreading. The container array is also only slightly modifying the flow direction. This phenomenon has already been observed by Rochoux et al. (2021) with the MNH-IBM model. It has important consequences for the pollutant plume deflection. Indeed, as shown in the observations and in several numerical results (Milliez and Carissimo 2007; Dejoan et al. 2010), the containers induce a deflection of the mean pollutant plume axis relative

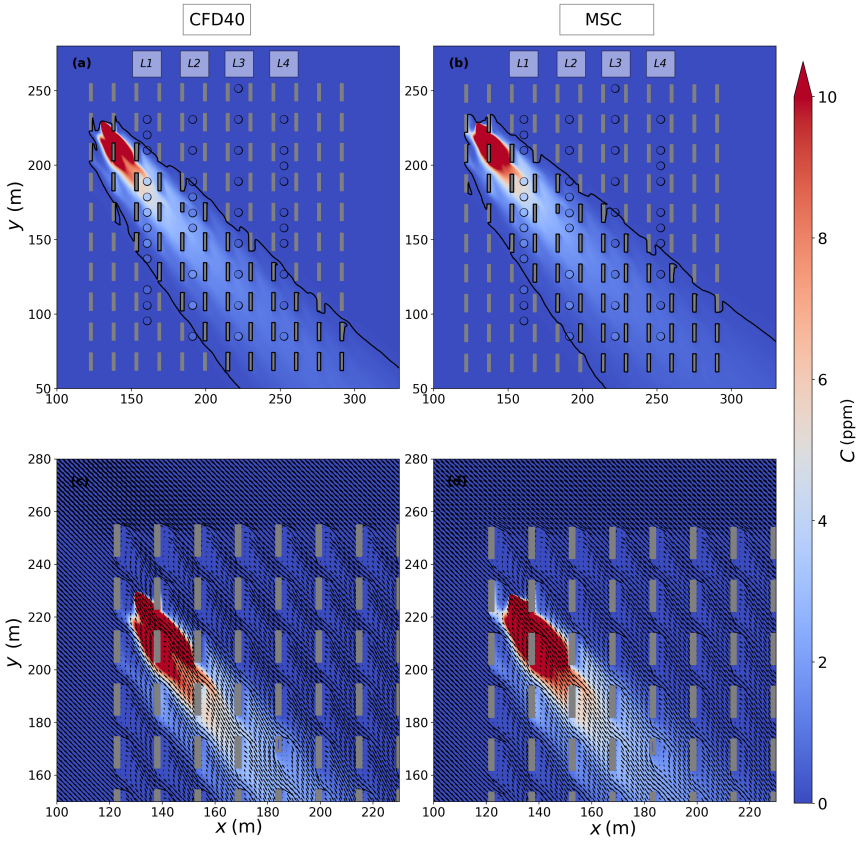


Fig. 10 Pollutant concentration averaged over 900 s at $z = 1.6$ m for the CFD40 (**a** and **c**) and the multiscale (**b** and **d**) configurations. The coloured circles indicate the observed values at the 40 PIDs probes. The full lines show the 0.1 ppm iso-line of pollutant concentration. The velocity vectors averaged over 900 s at $z = 1.6$ m for the CFD40 (**c**) and the multiscale (**d**) configurations are also displayed for a subdomain close to the inflow boundary in the lower line

to the inflow wind direction. For the MUST case 2681829, this deflection is particularly pronounced between container rows L to I (Fig. 8. of Milliez and Carissimo 2007), where the pollutant is channelled with the flow perpendicular to the x-axis of the container array. A comparison between our Fig. 10 and the Fig. 8. of Milliez and Carissimo (2007) shows that MNH-IBM underestimates the plume deflection close to the pollutant source location for all configurations. The reason can be found in the flow pattern. The velocity quivers show the presence of recirculation cells downstream of the containers but also of strong jets rushing between the containers. The pollutant plume is subject to a competition between the recirculation cells that drive it perpendicular to the x-axis (this happens at mast T for instance) and the jets that are almost aligned with the upstream wind. The jets, because of their

583 higher velocity, separate the different recirculation cells, the y-axis momen-
584 tum induced by the recirculation is broken and the pollutant is advected to
585 the next container street. The jets are therefore reducing the y-axis deflection
586 of the plume and its spreading on the horizontal directions. With MNH-IBM,
587 the jets are probably too strong and they cause an underestimation of the
588 pollutant plume deflection. We do not have a clear explanation of what causes
589 this phenomenon but it is possible that the lift effect that should be generated
590 by the elongated face of each container is underestimated. More investigations
591 should be carried on to properly explain this flaw. However, this is beyond the
592 scope of the present paper.

593 Figure 11 shows the 900-s-average concentration at $z = 1.6$ m along the
594 lines 1 (Fig. 11a), 2 (Fig. 11b), 3 (Fig. 11c), and 4 (Fig. 11d). The two CFD-
595 like configurations present very similar results and are analyzed together. For
596 probe lines 1, 2, and 3, the CFD-like configurations overestimate the maximum
597 value of pollutant concentration, which is located at the plume centreline. This
598 overestimation is more important for lines 1 and 2, i.e., close to the source
599 location. The left edge of the plume (from a wind flow point of view, i.e., right
600 of the figure) position is always well located. However, because the model is not
601 dispersive enough, the horizontal expansion of the plume is underestimated.
602 This has few consequences for line 1 where the right edge position of the plume
603 is well captured. But, when moving away from the release point (lines 2, 3,
604 and 4), the right edge position of the plume is shifted in space and pollutant
605 concentrations are underestimated at these locations. As a consequence, the
606 position of the maximum pollutant concentration is also shifted to the left
607 (from a wind flow point of view) for lines 2, 3, and 4. These observations are
608 consistent with those shown in Fig. 10 and highlight the main issue of the
609 CFD-like configurations, which are not sufficiently dispersive.

610 The MSC results are in slightly better agreement with the observations. For
611 lines 1 and 2, the edge of the plume is still well located and the maximum value
612 of pollutant concentration is less overestimated (especially for line 2) than for
613 the CFD-like configurations. It is in good agreement with the observations for
614 line 3 but underestimated for line 4. As for the CFD-like configurations, the
615 left edge of the plume is always well located, but when moving away from the
616 source, the concentration in the right side of the plume is underestimated and
617 the position of the maximum concentration is shifted in space. The dispersion
618 of the pollutant is however slightly better simulated than for the CFD-like
619 configurations. This is particularly true for lines 1 and 2, where MSC presents
620 fewer errors than the CFD-like configurations at the right edge of the plume
621 (left of the figure). This is consistent with the plume presented in Fig. 10.

622 Figure 12 shows the 900-s-average vertical profiles of pollutant concentra-
623 tion along mast T (Fig. 12a), towers B (Fig. 12b), and D (Fig. 12c). Tower
624 A is not taken into account because it is outside the dispersion plume extent
625 (see Fig. 2). Similar to Fig. 11, the two CFD-like configurations present very
626 similar results and are analyzed together.

627 For the CFD-like configurations, the pollutant concentration is overesti-
628 mated below $z = 12$ m at the mast T location, all along the vertical for tower

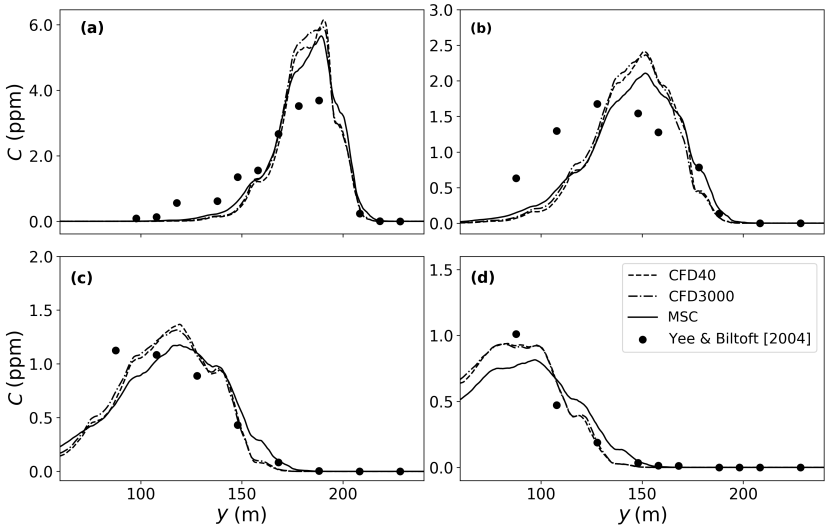


Fig. 11 900-s average pollutant concentration (C) at $z = 1.6$ m along the lines 1 (**a**), 2 (**b**), 3 (**c**), and 4 (**d**)

B, whereas it is underestimated for all probes at tower D. The agreement of the vertical profiles of pollutant concentration between the CFD-like configuration and the observations is poor but this can be expected in regards of the deficiencies in the horizontal plume spreading. Indeed, for the two CFD-like configurations, the mast T is located close to the plume centreline, where, because the configuration is not dispersive enough, these configurations overestimate the pollutant concentration. This lack of dispersion can also explain the concentration underestimation at tower D, located at the right edge of the pollutant plume.

For the MSC, the results are in better agreement with the observations at mast T, even if the pollutant concentration is also overestimated below $z = 10$ m. At tower B, the concentration is overestimated by a factor of 2 for all probes. For tower D, the multiscale results are improved compared with the CFD-like ones. However, the concentration is still underestimated compared with the observations. This is, once again, probably caused by the underestimation of the horizontal dispersion.

Overall, in terms of pollutant concentration, CFD-like and multiscale results differ only slightly and are both in good agreement with the observations. The MSC results agree slightly better with the observations than the CFD-like ones for both horizontal and vertical probes. Taking into account the large-scale turbulent structures of the ABL seems therefore to also improve the concentration results, but only slightly. Moreover, the results for towers B and D are still unsatisfactory with the MSC. These points are further discussed in Sect. 6.

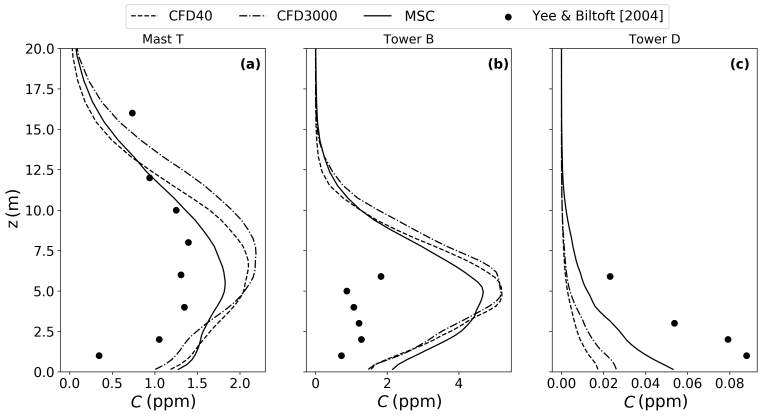


Fig. 12 Vertical profiles of 900-s-average pollutant concentration along mast T (**a**) and towers B (**b**), and D (**c**)

6 Discussion

The results presented in Sect. 5 show that MNH-IBM is able to qualitatively capture the observed pollutant concentrations for the selected MUST experiment. From a qualitative point of view, the MSC results are in better agreement with the observations than the CFD-like ones. In this section, the results are analyzed from a quantitative point of view and thoroughly discussed.

6.1 Skill Scores

The model performance for the average wind speed is evaluated with the hit rate (HR), adapted from Cox et al. (1998), it is expressed as the fraction of data where the averaged simulated wind speed is within a ± 1 m s^{-1} range from the observation:

$$HR = \frac{1}{N_t} \sum_{i=1}^{N_t} N_i \text{ with } N_i = \begin{cases} 1 \text{ if } \mid \overline{U_{p_i}} - \overline{U_{o_i}} \mid \leq \ 1\text{m s}^{-1} \\ 0 \text{ else} \end{cases}, \tag{4}$$

where N_t is the number of samples, and $\overline{U_p}$ and $\overline{U_o}$ are the simulated and observed time-averaged wind speed, respectively. A perfect model would result in $HR = 1$.

The model performance for the wind direction is evaluated with the scaled average angle difference (SAA) originally proposed by Calhoun et al. (2004):

$$SAA = \frac{\sum \left(\overline{U_{p_i}} \mid \overline{\alpha_{p_i}} - \overline{\alpha_{o_i}} \mid \right)}{N_t \langle \overline{U_p} \rangle}, \tag{5}$$

where $\overline{\alpha_p}$ and $\overline{\alpha_o}$ are the simulated and observed time-averaged wind directions, respectively. The brackets indicate averaging over the probes locations. A perfect model would result in $SAA = 0$.

The skill scores for the pollutant concentrations presented in Eqs. 6–9 are among those recommended by Hanna et al. (1993) to quantitatively measure the performance of a pollutant dispersion model. They include the fractional bias (FB), the fraction of simulation results within a factor of two of the observations ($FAC2$), the geometric mean bias (MG), and the geometric variance (VG):

$$FB = \frac{\langle\overline{C_p}\rangle - \langle\overline{C_o}\rangle}{0.5(\langle\overline{C_p}\rangle + \langle\overline{C_o}\rangle)}, \tag{6}$$

$$FAC2 = \frac{1}{N_t}\sum_{i=1}^{N_t} N_i \text{ with } N_i = \begin{cases} 1 \text{ if } \frac{1}{2} \leq \frac{\overline{C_{p_i}}}{\overline{C_{o_i}}} \leq 2 \\ 0 \text{ else} \end{cases}, \tag{7}$$

$$MG = \exp\left(\langle\ln(\overline{C_p})\rangle - \langle\ln(\overline{C_o})\rangle\right), \tag{8}$$

$$VG = \exp\left[\langle(\ln(\overline{C_o}) - \ln(\overline{C_p}))^2\rangle\right], \tag{9}$$

where $\overline{C_o}$ and $\overline{C_p}$ are the time-averaged observations and model simulation results, respectively. Chang and Hanna (2004) give the following values for an acceptable model performance:

$$FAC2 > 0.5,\ \text{-}0.3 < FB < 0.3,\ 0.7 < MG < 1.3,\ VG < 1.6\ ,$$

where $FAC2$, MG, and FB measure the systematic bias of the model results and indicate only the systematics errors, whereas VG measures the mean relative scatter of the data and accounts for both systematic and random errors. In order to reduce the influence of extremely low pollutant concentration values on MG and VG, the instrument threshold (0.04 ppm for the PIDs and 0.01 ppm for the UVIDs) is used as lower bound for C_o and C_p. The value of $FAC2$ is not sensitive to the variable distribution and is the most robust skill score according to Chang and Hanna (2004).

In contrast to Hanna et al. (1993) and Chang and Hanna (2004), the metrics FB and MG are here defined as the difference between model result and the observation. Therefore, FB (respectively MG) is positive (respectively above 1) when the model overestimates the pollutant concentrations; this corresponds to the standard definition of a model bias.

A graphic representation of the skill scores for the CFD40 (dashed bars), the CFD3000 (dotted bars), and the multiscale (crossed bars) configurations is given in Fig. 13. For the wind speed and the wind direction, the scores are calculated for the 27 probes available for that pollutant release among the sonic probes displayed in Fig. 2. A distinction is made between probes outside (in red) and within (in green) the container array. The probes outside the container array might be located upstream, above, or downstream of the containers. They are mounted on mast T, towers N, S and at the top level of towers A, B, and D. The probes within the container array are close to

the ground (UU, V, LANL2D, bottom level of towers A, B, and D). For the pollutant concentration, a distinction is made between horizontal (on lines 1 to 4) and vertical probes (mounted on mast T, towers A, B, and D). The scores for the horizontal and the vertical probes are shown in cyan and magenta, respectively. For each skill score, the result for all probes is shown in blue.

6.2 Wind Speed and Wind Direction

The hit rate for the wind speed is shown on Fig. 13a. Outside of the container array, CFD3000 and MSC present a perfect score of $HR = 1$, whereas the CFD40 has $HR = 0.92$. This is most probably because the CFD40 configuration has a model top at $z = 40$ m, which leads to an artificial overestimation of the wind speed above the containers, especially in the upper part of the domain (Fig. 9). Because the CFD-like configuration follows Franke et al. (2011) recommendations, this artificial wind speed overestimation is minimized and the hit rate remains satisfactory.

Inside the array, CFD40 presents $HR = 0.57$. This score is improved with CFD3000 where $HR = 0.71$. For the MSC, $HR = 0.79$ inside the array. These results show that a low top boundary affects the flow inside the array in a non-negligible way for the CFD-like configurations. Furthermore, accounting for the large-scale turbulent fluctuations enhances wind speed simulation within the container array. As a consequence, the hit rate for all probes is also improved using the MSC (0.74 for CFD40, 0.85 for CFD3000 and 0.89 for MSC).

For the wind direction outside of the container array, the SAA is rather satisfactory with similar values of 7.44, 7.92 and 7.92 for CFD40, CFD3000, and MSC, respectively. Contrary to the wind speed, the wind direction simulation, at least outside of the container array, is not improved with the MSC. Inside the container array, the SAA score is very poor for all configurations: 64, 62.92, and 62.12 for CFD40, CFD3000, and MSC, respectively. The slight improvement for MSC is negligible. Two points might reduce the importance of this bad score. First, the wind direction is varying quite rapidly over short distances. In these conditions, the wind direction simulations within the container array are expected to be difficult and not very accurate. Second, the probes available inside the array are not very representative. Indeed, as can be seen on Fig. 2, they are mostly located in two specific areas: in the recirculation cell of container L4 (UU and LANL2D probes) and around mast T (V probes). Despite these points, it is clear that, for all configurations, the model does not simulate correctly the overall wind direction in the container array. This could also be another reason for the difficulties encountered by the model in getting the plume deflection correct as shown in Fig. 10.

6.3 Pollutant Concentration

For the two CFD-like configurations, Fig. 13c shows that $FAC2 = 0.73$, 0.50, and 0.65 for the horizontal, the vertical, and all probes, respectively. This

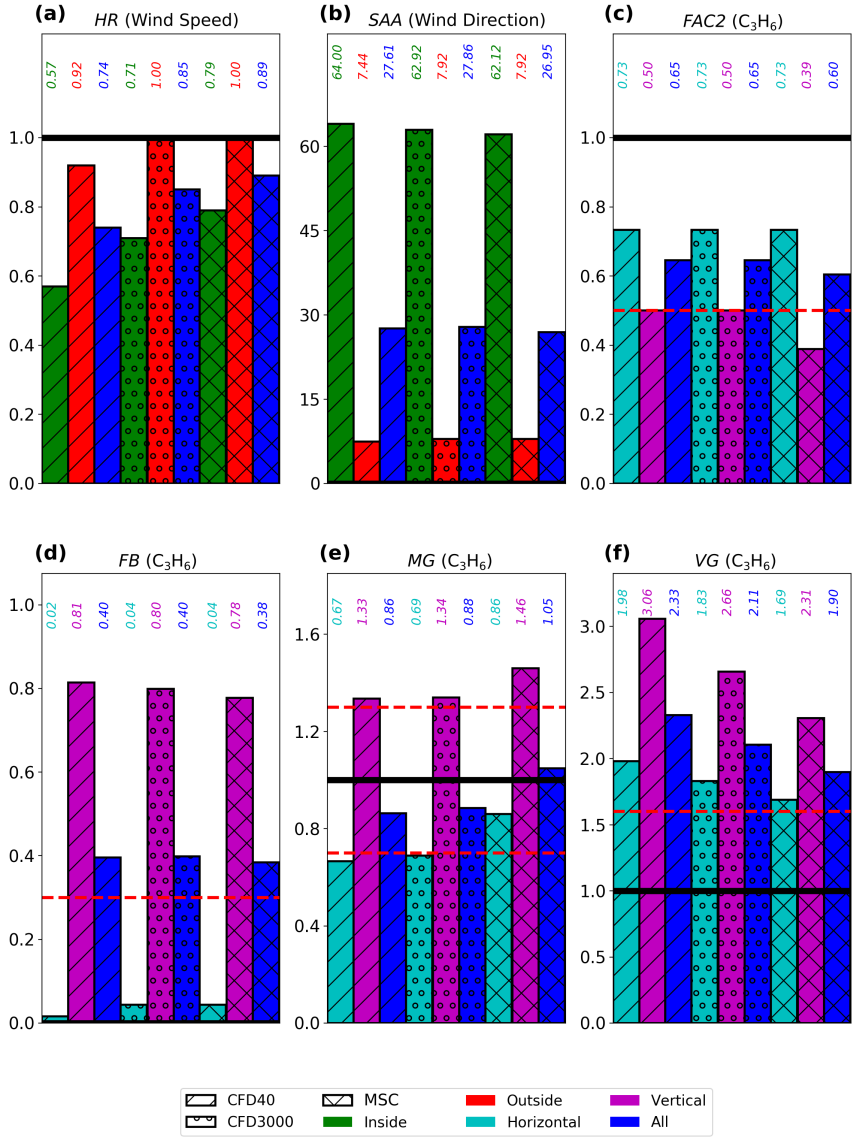


Fig. 13 Skill scores for the wind speed and the pollutant concentration for the CFD-like and MSC configurations. The thick horizontal black line indicates a perfect skill score. The dashed red lines indicate an acceptable skill score according to Chang and Hanna (2004)

is very satisfactory as the score for each probes ensemble is above or equal to the acceptable model performance threshold value of 0.5. The skill scores calculated in the present study cannot be compared with those from the lit-

erature (Milliez and Carissimo 2007) as the latter are obtained for a 200-s nearly-stationnary period filtering the large-scale turbulent fluctuations. The horizontal FB value is also very satisfactory with a value of 0.02 for CFD40 and 0.04 for CFD3000. However, the vertical FB values of 0.80 and 0.81 show that the CFD-like configurations strongly overestimate the concentration for the vertical probes. This overestimation is also found by looking at the value of MG (≈ 1.3) and at the vertical concentration profiles for Mast T and Tower B displayed in Fig. 12.

The MSC gives $FAC2 = 0.73$ for the horizontal probes. This good score is identical to the CFD-like configuration. The score drops to 0.39 for the vertical probes, which is below the acceptable value threshold. The total $FAC2$ value of 0.6 is satisfactory. The horizontal FB value is very close to the ideal value of 0. However, as for the CFD-like configurations, the vertical FB value of 0.79 shows that the MSC overestimates the concentration for the vertical probes. Similarly to the CFD-like configurations, this overestimation is confirmed by the value of MG (1.46) and by the vertical profiles displayed in Fig. 12.

The value of $FAC2$ does not show any improvement with the MSC. The score is worse for the vertical probes (0.39 versus 0.50 for the CFD-like configurations). These results are surprising because the pollutant concentration profiles presented in Figs. 11 and 12 show a slight but clear improvement with the MSC. The reason is simple: the multiscale and the CFD-like configurations present mostly differences where both are within or outside a factor of two of the observations, making impossible for the $FAC2$ parameter to distinguish which configuration is the best. A thorough analysis can be performed using the other metrics. For the horizontal probes, the MSC gives $MG = 0.86$, which is within the acceptable model range from Chang and Hanna (2004). This is not the case for the CFD-like configurations where $MG < 0.7$. A similar result is found for VG (1.69 versus 1.83 for CFD3000 and 1.98 for CFD40). The metrics MG and VG are sensitive to low pollutant concentration values, which can be found for probes close to the edge of the plume. In other terms, the experimental low pollutant concentrations are more accurately captured with the MSC than with the CFD-like ones, a result in agreement with the horizontal transects presented in Fig. 11.

Concerning the vertical probes, the probes at the bottom of tower B are within the $FAC2$ range for the CFD-like configurations but not for the multiscale one. For the probes at mast T (respectively tower D), the multiscale results are overall better than the CFD-like ones but the CFD-like results remain inside (respectively outside) the $FAC2$ range of the experimental values. As a result, the vertical $FAC2$ is better for the CFD-like configurations, even though other metrics (FB, VG) indicate that these configurations overestimate the vertical concentration more than the MSC. Overall, this example is a good reminder that it is safer to evaluate the model performance using several complementary metrics.

6.4 Influence of the Top Boundary Height for the CFD-like Configurations.

The CFD40 configuration has a low top boundary, as it is usually done in CFD. Even if this configuration respects the literature recommendations (Franke et al. 2011; Blocken 2015), this is not without consequences on the wind speed estimation. There is a small Venturi effect above the container array and the CFD3000 wind speed results are in better agreement with the observations than the CFD40 ones. This statement is true outside and inside the container array. However, no such conclusions can be drawn for the pollutant dispersion. The horizontal and vertical profiles such as most of the skill score estimators do not show a significant improvement in the pollutant dispersion simulation with the CFD3000 case. The model improvement is more significant, even if it remains slight, with the MSC. The pollutant dispersion results presented here are therefore more dependent on the large-scale turbulent structures of the ABL than of the top height of the domain boundary.

6.5 Plume Deflection Underestimation Impact on the Model Performance

The overall weaker model performance for the vertical probes can mostly be explained by the plume deflection underestimation and to a lesser extent by the vertical profiles sensitivity to the plume direction. The plume deflection underestimation has important consequences on the results accuracy as it is most probably responsible of the concentration overestimation at tower B. Indeed, tower B is located at the left edge of the plume (from a wind flow point of view, see Figs. 2 and 10) in the experiment but closer to the plume centreline in the presented numerical results. This phenomenon impacts the results accuracy in all configurations. The pollutant underestimation at tower D, located at the edge of the plume, is another consequence of the plume deflection underestimation.

The consequences of the plume deflection underestimation are also more important for the vertical profiles because they are sensitive to the plume direction (Milliez and Carissimo 2007). Indeed, if one or several profiles are located at the edge of the plume (as tower B and D in the present case), where the pollutant concentrations are low (and therefore difficult to simulate), a small imprecision in the plume direction impacts the simulated concentration. For the present study, few observed vertical profiles are available, which amplifies the impact of one single profile on the total skill score.

6.6 Pollutant Dispersion

The results presented in Sect. 5 show that the pollutant dispersion is underestimated. This flaw is found for all configurations but is more important for the CFD-like ones. The reason for this deficiency is not the advection scheme. First, because WENO5 is known to be a diffusive numerical scheme. Second,

because this drawback has been found regardless of the advection scheme (WENO5 or CEN4TH, not shown here). Like for the pollutant plume deflection underestimation, the dispersion underestimation is probably due to the difficulties of the model to simulate the wind direction in the array and to the strong jets rushing between the containers (Fig. 10).

6.7 Conclusion

The overall performance metrics show that performing a LES simulation of the MUST case using a MSC rather than a CFD-like one only slightly improves the pollutant concentration results. Accounting for the large ABL turbulent structures is therefore improving the numerical results accuracy for the pollutant dispersion but significantly less than what is reported in Wiersema et al. (2020) for the JU2003 field campaign in Oklahoma City. The main differences between both cases are the horizontal and vertical size distribution of the buildings. The MUST case presents an array of containers with uniform height, regular shape, and spacing, whereas downtown Oklahoma City presents important variations in buildings horizontal and vertical size, shape, and spacing. The present results show that the benefit of accounting for the large-scale ABL structures to simulate the pollutant dispersion in a city is dependent on the city specific configuration. In the MUST case, which represents an idealized city, this benefit is limited whereas, according to Wiersema et al. (2020), it is very important for JU2003.

7 Summary and Conclusion

In the present study, LESs are performed with the mesoscale atmospheric model Meso-NH to investigate the influence of the ABL turbulence on the mean flow, the turbulence, and the pollutant dispersion in the MUST idealized urban-like environment. The influence of a limited vertical model domain extent, which is usually used in CFD simulations, is also investigated. Three configurations are studied: two CFD-like configurations, with and without limited vertical extent, composed of a single high-resolution model domain where a steady velocity profile is imposed at the domain boundaries and a multiscale configuration, composed of four grid-nested domains with increasing horizontal resolution. Only the MSC accounts for all scales of atmospheric turbulence prevailing in the ABL. The building-like obstacles are represented using the IBM.

A new turbulence recycling method is successfully used to enhance the turbulence scale transition between two nested subdomains: the prognostic variable fluctuations from a vertical plane parallel to the inflow boundary are calculated with respect to a moving temporal average and added to the prognostic variable field at the inlet.

The wind characteristics such as the wind speed, the wind direction, and the TKE upstream of the container array are well reproduced with the MSC,

showing the efficiency of the turbulence downscaling from the meso-scale to the microscale as well as of the turbulence recycling method. Furthermore, contrary to the CFD-like configurations, the MSC is able to reproduce the mesoscale turbulent structures crossing the container array, allowing further investigation of their impact on the pollutant dispersion.

The accuracy of the numerical results is evaluated with various skill scores, including those recommended by Chang and Hanna (2004) for the pollutant concentration. The CFD-like configuration with a limited domain height tends to overestimate the wind speed, due to a small Venturi effect above the container array. This is not the case for the CFD-like configuration extending over the entire ABL. The MSC results are the ones in better agreement with the experimental measurements of Yee and Biltoft (2004) for the wind speed. All configurations show an equivalent good performance for the wind direction outside the container array but fail to simulate accurately the wind direction inside the array. Concerning the pollutant concentration, the two CFD-like configurations are almost identical, confirming that there is no need to solve the entire ABL in such configuration. The MSC presents only a slight improvement in terms of pollutant dispersion simulation. Overall, the present study shows that the microscale numerical simulation of wind speed and pollutant dispersion in an urban environment benefits from taking into account the ABL turbulence. However, this benefit is significantly less important than the one described by Wiersema et al. (2020) with the WRF model on the JU2003 field campaign in Oklahoma City. The MUST idealized city configuration overcomes the effects of a specific urban environment on the results. The present work shows that the general conclusion of Wiersema et al. (2020) can be verified in an idealized case. However, it also highlights that the specific configuration of the city seems to have a strong impact on the benefit of accounting for large ABL turbulent structures. For the MUST case, where obstacles have an uniform height, size, shape, and spacing, the benefit is limited. For the JU2003 case, where the buildings present important variations in buildings height, size, shape, and spacing, the benefit is important (Wiersema et al. 2020). It is also possible that idealized models using generic buildings like MUST or in Cheng and Castro (2002) are too simple to properly represent the complex phenomena that drive pollutant transport in real cities. In that case, the influence of parameters such as the presence of tall buildings, non-regular horizontal dimensions or spacing of the obstacles and their link with the ABL turbulence and pollutant dispersion simulation should be investigated by performing a study similar to the present work on a field experiment dataset where obstacles have different shape, height, and spacing, like Jack Rabbit II (Pirhalla et al. 2020; Mazzola et al. 2021).

In addition, it is worth mentioning that the present results are limited to a near-neutral case. For non-neutral atmospheric conditions, the ABL turbulence may have a different impact on the microscale structures of the urban canopy. This should be investigated in future studies, including the full radiative effects in the canopy.

This study also confirms that the IBM is a promising way to represent the flow interaction with buildings in atmospheric models for urban applications. But it also shows that the MNH-IBM model presents room for improvement. The most obvious flaw of the model is the plume deflection underestimation. A sensitivity study to the wall roughness or the law of the wall should be undertaken to better understand this flaw. This drawback directly impacts the pollutant dispersion simulation accuracy as it reduces the plume spreading compared with the observations, at least close to the pollutant release location.

More broadly, high-resolution numerical simulations of urban areas using the IBM appear as a suitable tool to calculate parameters such as cities drag coefficient to improve parametrizations in mesoscale atmospheric simulations.

Acknowledgements We are grateful to the three anonymous reviewers for their in-depth review and their constructive comments. We would like to thank the Defense Threat Reduction Agency (DTRA) for providing access to the MUST data. We would like to thank Mélanie Rochoux, Laëticia Thouron, Antoine Verrelle and Franck Auguste for the helpful discussions so as Quentin Rodier and Juan Escobar for their precious help with Meso-NH. Tim Nagel's postdoctoral position was funded by the FCS-STAE foundation and the IRT Saint-Exupéry, Toulouse, under the PPM project and by the EU LIFE climate change adaptation 2018 project Generate REsiliENt actions agaiNst the HEat islAnd effect on uRban Territory (Green Heart; LIFE18 CCA/FR/001150).

References

Allwine K, Leach M, Stockham L, Shinn J, Hosker R, Bowers J, Pace J (2004) J7. 1 Overview of Joint Urban 2003–an atmospheric dispersion study in Oklahoma City

Allwine KJ, Flaherty JE (2006) Joint Urban 2003: Study overview and instrument locations. Pacific Northwest National Lab.(PNNL), Richland, WA (United States), Tech rep

Auguste F, Réa G, Paoli R, Lac C, Masson V, Cariolle D (2019) Implementation of an immersed boundary method in the Meso-NH v5.2 model: applications to an idealized urban environment. Geosci Model Dev 12(6):2607–2633

Auguste F, Lac C, Masson V, Cariolle D (2020) Large-eddy simulations with an immersed boundary method: Pollutant dispersion over urban terrain. Atmosphere 113(11):200–200

Biltoft CA (2001) Customer report for mock urban setting test. DPG Document Number 8-CO-160-000-052. Prepared for the Defence Threat Reduction Agency, Tech rep

Blocken B (2015) Computational Fluid Dynamics for urban physics: Importance, scales, possibilities, limitations and ten tips and tricks towards accurate and reliable simulations. Build Environ 91:219–245

Calhoun R, Gouveia F, Shinn J, Chan S, Stevens D, Lee R, Leone J (2004) Flow around a complex building: Comparisons between experiments and a Reynolds-averaged Navier–Stokes approach. J Appl Meteorol 43(5):696–710

Chang JC, Hanna SR (2004) Air quality model performance evaluation. Meteorol Atmos Phys 87(1-3):167–196

962 Cheng H, Castro IP (2002) Near wall flow over urban-like roughness.
963 Boundary-Layer Meteorol 104(2):229–259
964 Colella P, Woodward PR (1984) The piecewise parabolic method (ppm) for
965 gas-dynamical simulations. J Comput Phys 54(1):174–201
966 Couvreux F, Bazile E, Rodier Q, Maronga B, Matheou G, Chinita MJ, Ed-
967 wards J, van Stratum BJ, van Heerwaarden CC, Huang J, et al. (2020)
968 Intercomparison of large-eddy simulations of the antarctic boundary layer
969 for very stable stratification. Boundary-Layer Meteorol 176(3):369–400
970 Cox R, Bauer BL, Smith T (1998) A mesoscale model intercomparison. Bull
971 Am Meteorol Soc 79(2):265–284
972 Cuxart J, Bougeault P, Redelsperger JL (2000) A turbulence scheme allowing
973 for mesoscale and large-eddy simulations. Q J R Meteorol Soc 126(562):1–30
974 Dauxois T, Peacock T, Bauer P, Caulfield C, Cenedese C, Gorlé C, Haller G,
975 Ivey G, Linden P, Meiburg E, et al. (2021) Confronting grand challenges in
976 environmental fluid mechanics. Phys Rev Fluid 6(2):020,501
977 Dejoan A, Santiago J, Martilli A, Martin F, Pinelli A (2010) Comparison
978 between large-eddy simulation and Reynolds-averaged Navier–Stokes com-
979 putations for the must field experiment. Part II: effects of incident wind
980 angle deviation on the mean flow and plume dispersion. Boundary-Layer
981 Meteorol 135(1):133–150
982 Durran DR (1989) Improving the anelastic approximation. J Atmos Sci
983 46(11):1453–1461
984 Franke J, Hellsten A, Schlunzen KH, Carissimo B (2011) The cost 732 best
985 practice guideline for cfd simulation of flow in the urban environment: a
986 summary. Int J Environ Pollut 44(1-4):419–427
987 Gal-Chen T, Somerville RC (1975) On the use of a coordinate transformation
988 for the solution of the Navier–Stokes equations. J Comput Phys 17(2):209–
989 228
990 García-Sánchez C, Gorlé C (2018) Uncertainty quantification for microscale
991 CFD simulations based on input from mesoscale codes. J Wind Eng Ind
992 Aerodyn 176:87–97
993 García-Sánchez C, van Beeck J, Gorlé C (2018) Predictive large eddy simula-
994 tions for urban flows: Challenges and opportunities. Build Environ 139:146–
995 156
996 Hanna S, Chang J, Strimaitis D (1993) Hazardous gas model evaluation with
997 field observations. Atmos Environ A, Gen Top 27(15):2265–2285
998 Honnert R, Masson V, Lac C, Nagel T (2021) A theoretical analysis of mixing
999 length for atmospheric models from micro to large scales. Front Earth Sci
1000 8:582,056
1001 Iaccarino G, Verzicco R (2003) Immersed boundary technique for turbulent
1002 flow simulations. Appl Mech Rev 56(3):331–347
1003 Jabouille P, Guivarch R, Kloos P, Gazen D, Gicquel N, Giraud L, Asencio N,
1004 Ducrocq V, Escobar J, Redelsperger JL, et al. (1999) Parallelization of the
1005 french meteorological mesoscale model Méso-NH. In: European Conference
1006 on Parallel Processing, Springer, pp 1417–1422

Kataoka H, Mizuno M (2002) Numerical flow computation around aerolastic 3D square cylinder using inflow turbulence. Wind Struct Int J 5(2/4):379–392

Kim W, Choi H (2019) Immersed boundary methods for fluid-structure interaction: A review. Int J Heat Fluid Flow 75:301–309

Lac C, Chaboureau P, Masson V, Pinty P, Tulet P, Escobar J, Leriche M, Barthe C, Aouizerats B, Augros C, et al. (2018) Overview of the Meso-NH model version 5.4 and its applications. Geosci Model Dev 11:1929–1969

Lin SJ, Rood RB (1996) Multidimensional flux-form semi-lagrangian transport schemes. Mon Weather Rev 124(9):2046–2070

Lund TS, Xiohua W, Squires KD (1998) Generation of turbulent inflow data for spatially developing boundary layer simulations. J Comput Phys 140(2):233–258

Lundquist KA, Chow FK, Lundquist JK (2010) An immersed boundary method for the Weather Research and Forecasting model. Mon Weather Rev 138(3):796–817

Lundquist KA, Chow FK, Lundquist JK (2012) An immersed boundary method enabling large-eddy simulations of flow over complex terrain in the WRF model. Mon Weather Rev 140(12):3936–3955

Lunet T, Lac C, Auguste F, Visentin F, Masson V, Escobar J (2017) Combination of WENO and explicit Runge–Kutta methods for wind transport in the Meso-NH model. Mon Weather Rev 145(9):3817–3838

Maronga B, Gryschka M, Heinze R, Hoffmann F, Kanani-Sühring F, Keck M, Ketelsen K, Letzel MO, Sühring M, Raasch S (2015) The parallelized large-eddy simulation model (PALM) version 4.0 for atmospheric and oceanic flows: model formulation, recent developments, and future perspectives. Geosci Model Dev 2:2514–2551

Masson V, Le Moigne P, Martin E, Faroux S, Alias A, Alkama R, Barbu A, Boone A, Bouyssel F, et al. (2013) The SURFEXv7.2 land and ocean surface platform for coupled or offline simulation of earth surface variables and fluxes. Geosci Model Dev 6:929–960

Mazzola T, Hanna S, Chang J, Bradley S, Meris R, Simpson S, Miner S, Gant S, Weil J, Harper M, et al. (2021) Results of comparisons of the predictions of 17 dense gas dispersion models with observations from the Jack Rabbit II chlorine field experiment. Atmos Environ 244:117,887

Mesinger F, Arakawa A (1976) Numerical methods used in the atmospheric models

Milliez M, Carissimo B (2007) Numerical simulations of pollutant dispersion in an idealized urban area, for different meteorological conditions. Boundary-Layer Meteorol 122(2):321–342

Muñoz-Esparza D, Kosović B, Mirocha J, van Beeck J (2014) Bridging the transition from mesoscale to microscale turbulence in numerical weather prediction models. Boundary-Layer Meteorol 153(3):409–440

Muñoz-Esparza D, Kosović B, van Beeck J, Mirocha J (2015) A stochastic perturbation method to generate inflow turbulence in large-eddy simulation models: Application to neutrally stratified atmospheric boundary layers.

Phys Fluids 27(3)
Park SB, Baik JI, Han BS (2015a) Large-eddy simulation of turbulent flow in a densely built-up urban area. Environ Fluid Mech 15(2):235–250
Park SB, Baik JI, Lee SH (2015b) Impacts of mesoscale wind on turbulent flow and ventilation in a densely built-up urban area. J Appl Meteorol Clim 54(4):811–824
Pirhalla M, Heist D, Perry S, Hanna S, Mazzola T, Arya SP, Aneja V (2020) Urban wind field analysis from the Jack Rabbit II special sonic anemometer study. Atmos Environ 243:117,871
Rochoux M, Thouron L, Rea G, Auguste F, Jaravel T, Vermorel O (2021) Large-eddy simulation multi-model comparison of the MUST trial 2681829. Technical report - tr-cmgc-21-72
Roth M (2000) Review of atmospheric turbulence over cities. Q J R Meteorol Soc 126(564):941–990
Skamarock WC (2004) Evaluating mesoscale NWP models using kinetic energy spectra. Mon Weather Rev 132(12):3019–3032
Skamarock WC, Klemp JB, Dudhia J, Gill DO, Barker DM, Wang W, Powers JG (2008) A description of the advanced research WRF version 3. NCAR technical note-475+ str
Stein J, Richard E, Lafore JP, Pinty J, Asencio N, Cosma S (2000) High-resolution non-hydrostatic simulations of flash-flood episodes with grid-nesting and ice-phase parameterization. Meteorol Atmos Phys 72(2-4):203–221
Sussman M, Smereka P, Osher S (1994) A level set approach for computing solutions to incompressible two-phase flow
Tominaga Y, Stathopoulos T (2013) CFD simulation of near-field pollutant dispersion in the urban environment: A review of current modeling techniques. Atmos Environ 79:716–730
Tseng YH, Ferziger JH (2003) A ghost-cell immersed boundary method for flow in complex geometry. J Comput Phys 192(2):593–623
Wiersema DJ, Lundquist KA, Chow FK (2020) Mesoscale to microscale simulations over complex terrains with the immersed boundary method in the weather research and forecasting model. Mon Weather Rev 148(2):577–595
Yang G, Causon D, Ingram D, Saunders R, P B (1997) A cartesian cut cell method for compressible flows. Part A: Static body problems. Aeronaut J 101(1002):47–56
Yee E, Biltoft CA (2004) Concentration fluctuation measurements in a plume dispersing through a regular array of obstacles. Boundary-Layer Meteorol 111(3):363–415
Zängl G, Gantner L, Hartjenstein G, Noppel H (2004) Numerical errors above steep topography: A model intercomparison. Meteorol Z 13(2):69–76